Assessing Scale Effects in Solitary Wave-Induced Boulder Transport Experiments via High-Fidelity SPH Simulations

YICHEN JU[1] AND IRA DIDENKULOVA[1]

[1]*Department of Mathematics, University of Oslo*
yichencj@uio.no

Understanding boulder transport by solitary waves is crucial for coastal hazard assessment, but small-scale experiments are limited by scale effects, complicating extrapolation to real-world conditions. This study utilizes the high-fidelity Smoothed Particle Hydrodynamics (SPH) solver, DualSPHysics, to investigate these scale effects numerically. The model is first validated against small-scale laboratory experiments, successfully replicating wave profiles and boulder displacement trends for various geometries. Subsequently, the simulations are extended to a large-scale scenario, scaled up by a factor of 20, to analyze transport dynamics in a more realistic, inertia-dominated regime. Results show that while fundamental transport mechanisms scale consistently, the large-scale simulations correct certain discrepancies observed at the small scale. Notably, for a tall boulder geometry where the small-scale simulation deviated from experimental trends, the large-scale model accurately predicted the transport behavior, suggesting the SPH framework can better capture dominant physical forces at prototype scales. This work highlights the capability of SPH to bridge the gap between laboratory models and real-world phenomena, establishing it as a robust tool for assessing coastal hazards.

1. INTRODUCTION

Boulder transport on coastlines, especially that induced by tsunamis or solitary waves, has long been recognized as a critical indicator of extreme hydrodynamic events. Understanding the mechanisms behind such boulder displacements is not only essential for post-event hazard assessment but also for the design and resilience of coastal infrastructure. While field studies have identified massive coastal boulders displaced by historic tsunami waves [1], the underlying hydrodynamic processes and the interplay between wave characteristics, boulder properties, and seabed conditions remain partially understood [2].

Previous research has utilized both laboratory experiments and numerical modeling to investigate the dynamics of solitary wave-induced boulder transport [3] [4]. Several experimental studies have highlighted the role of boulder shape [3][5], wave impact type [6], and wave breaking position in determining transport behavior. Parameters such as Froude number and submergence factor have been found influential in the transport dynamics [7], and the transport mechanisms—such as rolling, sliding, or entrainment by surge—can vary substantially with environmental and geometric conditions [8][9]. Furthermore, bottom friction, slope material, and porosity have been shown to modulate transport distance and thresholds [10][11][12]. Physical flume experiments, such as those performed by [13], have revealed the role of factors like boulder geometry, wave breaking location, and the presence of sediment in enhancing or hindering transport. However, due to such experiments are restricted to small domains.

Small-scale experiments are often influenced by physical constraints and artifacts such as boundary effects, artificial damping, surface tension, and scale-dependent sediment behavior, significantly altering wave-particle interactions [4]. Additionally, the transport of boulders involves complex factors such as the wave-facing area, drag forces, and boulder transport modes—rolling, sliding, or saltating—which are difficult to investigate systematically in laboratory setups [4]. The interplay of these parameters leads to considerable uncertainties when extrapolating experimental findings to real-world conditions[5]. To overcome these limitations and uncertainties, researchers increasingly employ numerical methods.

Among these numerical techniques, Smoothed Particle Hydrodynamics (SPH), a mesh-free Lagrangian method initially developed in astrophysics [14], has proven effective for simulating highly nonlinear free-surface flows and wave breaking phenomena [15] [16] [17]. SPH allows flexible modeling of nonlinear wave dynamics, making it suitable for studying wave-induced boulder transport. The DualSPHysics framework, optimized for GPU computing, has been widely validated and used extensively in coastal engineering applications [18].

Nevertheless, traditional SPH methods, including earlier implementations of DualSPHysics, suffer from numerical artifacts such as non-physical energy dissipation, particle inconsistency, and inadequate momentum transfer conservation, especially in dynamic free-surface flows [19]. Recent developments like the

Enhanced DualSPHysics framework have introduced improvements, including higher-order kernel interpolations, enhanced density reinitialization schemes, and advanced formulations for pressure and viscosity terms, significantly improving physical accuracy and numerical stability [20].

Furthermore, [21] demonstrated SPH's capability in large-scale coastal modeling through accurate simulations of wave breaking over barred beach profiles. These simulations showcased SPH's effectiveness in reproducing critical hydrodynamic processes and provided a scalable tool for practical engineering applications.

In this study, we aim to leverage DualSPHysics to simulate solitary wave-induced boulder transport on a large-scale coastal scene, overcoming the limitations of small-scale experimental setups. Initially, we validate our simulation approach by replicating small-scale experiments and subsequently scale the model for extensive domain simulations, where practical experiments are difficult.

2. NUMERICAL EXPERIMENT SETUP

The numerical simulations presented in this study are designed to replicate and build upon previous physical experiments[13]. This section details the setup of the numerical model, encompassing the wave flume geometry, the methodology for solitary wave generation, the characteristics of the boulders used, and the configurations investigated.

The simulations were performed in a numerical wave flume configured to be analogous to the small-scale laboratory flume used in the reference experiments. The computational domain representing the flume has a total length of 3 m, a width of 0.1 m, and an overall height of 0.2 m. This domain includes a horizontal bed section extending for 1.65 m from the wave generation area, followed by a 1 : 10 slope (approximately 5.71°). The slope has a horizontal projection length of 1.32 m. The numerical flume was filled with water to a still water depth (h_w) of 0.05 m.

Solitary waves were generated at one end of the numerical flume using a virtual piston-type wavemaker. The motion of this piston is dictated by the Boussinesq theory for solitary wave generation [22][23] [24]. The target solitary waves were generated with a relative amplitude (a/h_w) of 0.5, corresponding to a wave amplitude (a) of 0.025 m for the 0.05 m water depth. The surface elevation $\eta(x)$ of the generated solitary wave, consistent with Boussinesq theory [22], can be described by:

$$\eta(x) = a \cdot \text{sech}^2 \left(\sqrt{\frac{3a}{4h_w(1 + a/h_w)}} \frac{x}{h_w} \right)$$

where x is the coordinate in the direction of wave propagation. In the subsequent phase of the simulation, these waves were propagated towards a beach where they broke on the shore, providing a canonical example of collapsing wave breaking.

The investigation focused on the interaction of these waves with submerged boulders. These boulders were modelled as rigid rectangular objects with a density of $\rho_b = 2015 \, \text{kg/m}^3$, mirroring the concrete boulders of the physical experiments. Four specific boulder geometries were simulated, defined by their length (L, in wave propagation direction), width (W, perpendicular to wave propagation), and height (H):

- **B111**: $L = 1 \, \text{cm}$, $W = 1 \, \text{cm}$, $H = 1 \, \text{cm}$
- **B112**: $L = 1 \, \text{cm}$, $W = 1 \, \text{cm}$, $H = 2 \, \text{cm}$

- **B121**: $L = 1 \, \text{cm}$, $W = 2 \, \text{cm}$, $H = 1 \, \text{cm}$
- **B211**: $L = 2 \, \text{cm}$, $W = 1 \, \text{cm}$, $H = 1 \, \text{cm}$

In each simulation, a single boulder was placed on the 1 : 10 slope, which was modelled as a smooth, impermeable boundary. The boulders were positioned at five different initial locations relative to the incipient wave breaking point (X_b). The ratio X_{B0}/X_b (initial boulder position X_{B0} to wave breaking location X_b) was used to define these locations: $X_{B0}/X_b = 1.0$ (at breaking point), and approximately 1.025 (5 cm shoreward), 1.05 (10 cm shoreward), 0.975 (5 cm seaward), and 0.95 (10 cm seaward of X_b).

A total of 20 distinct simulation cases were conducted, covering all combinations of the four boulder types and their five initial positions on the slope. The dynamics of the boulder and the surrounding fluid were analyzed for each case.
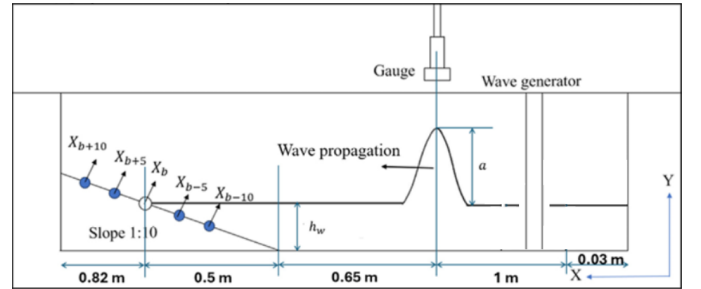

Fig. 1. Setup of the experiment.

3. NUMERICAL METHODOLOGY

The present simulations were conducted using the open-source mesh-free solver DualSPHysics[17, 18], which is based on the Smoothed Particle Hydrodynamics (SPH) method. SPH is a fully Lagrangian approach that solves the Navier–Stokes equations by discretizing the fluid domain into a set of moving particles. Each particle carries its own physical quantities such as position, velocity, pressure, and density, and interacts with neighboring particles through a smoothing kernel.

The governing equations of an incompressible, viscous fluid in Lagrangian form are given by:

$$\frac{d\rho}{dt} = -\rho \nabla \cdot \mathbf{v}, \tag{1}$$

$$\frac{d\mathbf{v}}{dt} = -\frac{1}{\rho} \nabla p + \nu \nabla^2 \mathbf{v} + \mathbf{g}, \tag{2}$$

where ρ is the fluid density, $\mathbf{v}$ is the velocity vector, p is the pressure, ν is the kinematic viscosity, and $\mathbf{g}$ is the gravitational acceleration.

In SPH, these equations are discretized using kernel interpolation. Any scalar field A at a particle position $\mathbf{r}_a$ is approximated as:

$$A(\mathbf{r}_a) = \sum_b \frac{m_b}{\rho_b} A_b W(\mathbf{r}_a - \mathbf{r}_b, h), \tag{3}$$

where m_b and ρ_b are the mass and density of the neighboring particle b, and W is a smoothing kernel function with compact support defined by the smoothing length h.

The discretized continuity and momentum equations in SPH formulation become[25]:

$$\frac{d\rho_a}{dt} = \sum_b m_b (\mathbf{v}_a - \mathbf{v}_b) \cdot \nabla_a W_{ab}, \qquad (4)$$

$$\frac{d\mathbf{v}_a}{dt} = -\sum_b m_b \left(\frac{p_a}{\rho_a^2} + \frac{p_b}{\rho_b^2} + \Pi_{ab} \right) \nabla_a W_{ab} + \mathbf{g}, \qquad (5)$$

where subscripts a and b denote the target and neighboring particles, respectively, and Π_{ab} is the artificial viscosity term[18] introduced to enhance numerical stability and damp spurious oscillations.

In this study, the Wendland kernel [26] was employed for kernel interpolation, owing to its high stability and reduced numerical noise compared to traditional kernels such as the cubic spline. The Wendland C^2 kernel function in three dimensions is given by:

$$W(q,h) = \alpha \left(1 - \frac{q}{2} \right)^4 (2q + 1), \quad 0 \le q \le 2, \qquad (6)$$

where $q = \frac{|\mathbf{r}_a - \mathbf{r}_b|}{h}$ is the normalized inter-particle distance, h is the smoothing length, and the normalization factor in three dimensions is $\alpha = \frac{21}{16\pi h^3}$. The kernel has compact support within a radius of $2h$, ensuring that each particle only interacts with neighbors within this range.

The Wendland kernel offers C^2 continuity, compact support, and increased robustness against particle disorder. These properties improve the stability and accuracy of pressure and force evaluations, making the kernel particularly well-suited for free-surface flows and fluid–structure interactions in SPH simulations.

The symplectic algorithm is employed for the time integration of the fluid equations, providing stability and energy conservation over long simulations. Variable time steps are adopted based on the Courant–Friedrichs–Lewy (CFL) condition [18]:

$$\Delta t = C_{\text{CFL}} \min \left(\Delta t_f, \Delta t_{cv} \right), \qquad (7)$$

$$\Delta t_f = \min_a \left(\sqrt{\frac{h}{\left| \frac{d\mathbf{v}_a}{dt} \right|}} \right), \quad \Delta t_{cv} = \min_a \left(\frac{h}{c_s + \max_b \left| \frac{h \mathbf{v}_{ab} \cdot \mathbf{r}_{ab}}{r_{ab}^2 + \eta^2} \right|} \right), \qquad (8)$$

where h is the smoothing length, $\mathbf{v}_{ab} = \mathbf{v}_a - \mathbf{v}_b$, $\mathbf{r}_{ab} = \mathbf{r}_a - \mathbf{r}_b$, and η is a small regularization parameter. The coefficient C_{CFL} is typically set to 0.1 for numerical stability. A small number of Euler predictor steps were applied initially to support velocity initialization [27]. The minimum time step was dynamically determined based on particle spacing and speed of sound, with a safety coefficient of 0.05.

To model viscous effects, artificial viscosity [28] was employed with a coefficient of 0.01, providing additional numerical damping to stabilize the simulation. Building on the findings of Altomare et al. (2023)[21], who emphasize the role of viscous effects in free surface wave breaking and recommend a higher viscosity parameter, the present study adopts a value of 0.025 as the most appropriate setting for improved model performance. Density diffusion was implemented using the full Fourtakas model[29], with a diffusion coefficient of 0.1, effectively mitigating spurious density fluctuations. Particle shifting was disabled to preserve realistic particle motion[18, 30], especially near boundaries and interfaces.

Boundary conditions were treated using the modified dynamic boundary condition (mDBC) approach[31], which improves consistency between fluid and boundary particle interactions. This method was applied to both static and dynamic bodies, including a fixed beach and a floating boulder.

Solitary waves were generated using the `piston_solitary` module in DualSPHysics[18], which follows the Boussinesq-type theory of Goring (1978)[22]. The wave paddle moved along the x-axis, producing a solitary wave with a height of 0.025 m in a water depth of 0.05 m. Motion data were recorded at $x = 1.03$ m for elevation analysis.

Rigid body dynamics were resolved through coupling with the Chrono engine. The floating body was modeled using the Chrono-based solver[32], enabling realistic collision handling and six-degree-of-freedom motion. Contact was treated as non-smoothed, with a collision overlap threshold set to $0.25 \Delta p$.

The contact dynamics between the boulder and the slope are managed by the Project Chrono physics engine using a Coulomb friction model. A critical input for this model is the kinetic friction coefficient (Kfric, or μ_k).

We considered using the friction coefficient (λ) from the reference study[13], where the author notes the value was "evaluated in experimental results." However, the paper does not explicitly elaborate on how this measurement was performed—for instance, whether it was under dry, wet, or fully submerged conditions. This lack of methodological detail makes it difficult to ascertain the precise physical meaning of λ and whether it represents a fundamental material property or an effective coefficient specific to their unstated experimental setup.

Given this ambiguity, we determined that the more rigorous and transparent approach was to use a fundamental material characteristic as required by the Chrono engine. We therefore defined Kfric based on established physical principles. Published literature values for this kinetic friction coefficient show significant variability, typically ranging from 0.4 to 0.7, depending on factors such as surface roughness and moisture [33, 34]. Due to this inherent variability and the unquantified surface conditions of the experiment, the Kfric was treated as a calibration parameter. A sensitivity analysis was performed by running simulations with several Kfric values within this physically plausible range. The values that yielded the best agreement between the simulated boulder displacement and the experimental data were determined to be 0.6 for the PMMA slope and 0.58 for concrete boulder.

The total simulation time was set to 6 s, with results output every 0.0075 s. This numerical setup ensures a stable and accurate representation of wave-body interactions under solitary wave forcing.

4. VALIDATION WITH SMALL-SCALE EXPERIMENT

To validate the accuracy and reliability of the *DualSPHysics* solver in replicating experimentally observed wave behavior, we first reproduced a small-scale water tank experiment previously conducted by Pin-Tzu Su [13]. While the physical experiment generated a solitary wave through the impact of a falling block, our numerical model replicated the same wave profile using a piston-type wave generator. This approach allowed us to directly compare the wave elevation measured at a fixed probe location in the physical flume with the data generated by our simulation.

As shown in Figure 2, the numerical results closely match the experimental data in both amplitude and waveform. The

rise and decay slopes of the solitary wave are well captured, particularly near the crest. Notably, the peak amplitude and overall shape of the wave profile are accurately reproduced.

To quantitatively assess the agreement, the peak elevation error between the simulation and experimental results is computed as:

$$\text{Error}_{\text{peak}} = \left| h_{\text{sim}}^{\max} - h_{\text{exp}}^{\max} \right| = 0.000755\,\text{m} \quad (3.03\%).$$

In this simulation, wave generation is performed at the center of the domain (0.53 m from left end), rather than at the boundary. This approach is physically valid for solitary waves, as their properties—including waveform and energy content—are uniquely determined by the wave amplitude. Moreover, since solitary waves are localized, translating the generation point does not alter their intrinsic characteristics. This setup is particularly suitable for *DualSPHysics*, where long-distance wave propagation can introduce non-physical energy diffusion due to numerical dissipation [21]. By generating the wave at the center, we ensure that the solitary wave reaches the boulder impact region with minimal numerical distortion, thereby preserving both its energy content and impact behavior.
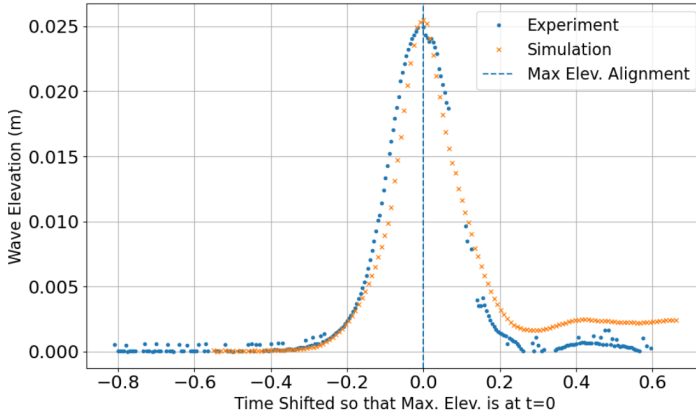

Fig. 2. Comparison of wave elevation between experiment and DualSPHysics simulation. The time axis has been shifted so that the maximum wave elevation occurs at $t = 0$. The simulation uses $H/d_p = 0.025/0.00125 = 20$.

This wave further propagates toward the coast impacting the boulders placed at different distances relative to the wave breaking point. The next figures 3 4 6 5 describe the boulder displacement caused by the breaking solitary wave.

For Boulder 111, the simulation closely matches the experimental data at pre-breaking locations and breaking point but diverges slightly further away from the breaking point. The experimental displacement initially increases slightly after $X = 1.00$ position, while the simulated data shows an immediate decline. Nevertheless, the overall decay rate is similar. This discrepancy may result from the cumulative dissipation of wave energy caused by numerical scheme as it propagates further down the slope.

In the case of Boulder 211, which shares the same impact area as Boulder 111 but has twice the mass and a larger frictional surface, both the simulation and the experiment exhibit minimal displacement, as expected. The simulation shows an earlier rise and a prematurely decreasing trend in displacement. This behavior may be attributed to a forward-shifted wave breaking

point, potentially caused by insufficient spatial resolution. Nevertheless, the simulation accurately captures the characteristic rise and subsequent drop in displacement.

For Boulder 121, the displacement was observed to be highly sensitive to the boulder's initial position, particularly when located near the wave breaking point. The resolution of the simulation significantly influences the intersection point between the wave surface and the slope, directly affecting the dynamics around wave breaking. Additionally, the experimental data for $X = 0.975$ and $X = 1.00$ showed substantial variability, suggesting that measurement uncertainty may also contribute to the observed mismatch in the central region. In contrast, the simulation accurately predicts behavior at the front and rear positions.

Finally, for Boulder 112, the results further highlight the influence of proximity to the wave breaking point. Whether the boulder undergoes overturning is governed by its initial distance from the breaking crest. The numerical resolution also affects how water interacts beneath the boulder during such overturning. Despite some local discrepancies, the simulation successfully captures the overall decreasing trend at positions $X = 1.00, 1.025,$ and 1.05.
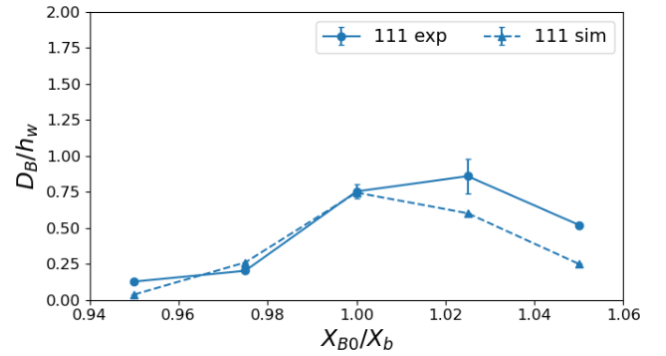

Fig. 3. Boulder 111: Comparison of boulder displacement between experiment and *DualSPHysics* simulation.
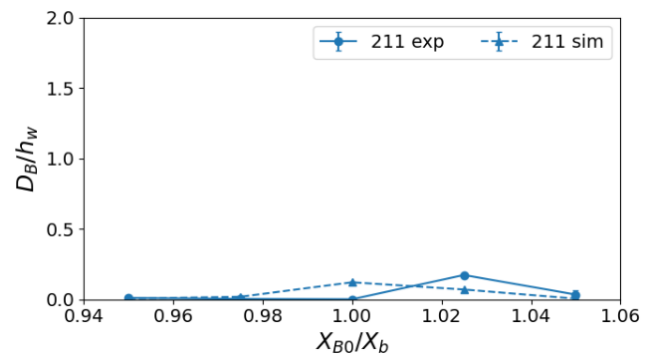

Fig. 4. Boulder 211: Comparison of boulder displacement between experiment and *DualSPHysics* simulation.

5. EXTENSION TO LARGE-SCALE SCENARIOS

The validation of DualSPHysics with small-scale experiments provides a strong foundation for investigating solitary wave-induced boulder transport in scenarios that are more representative of real-world coastal environments. Physical experiments at
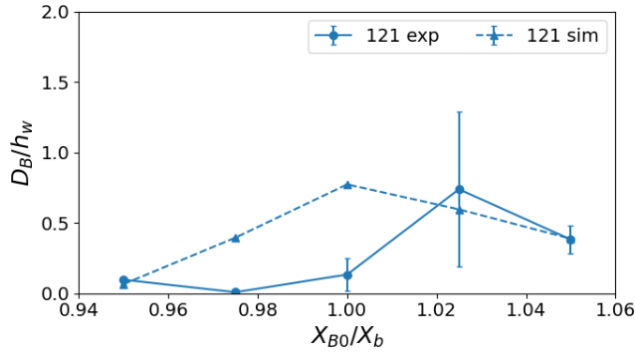
Fig. 5. Boulder 121: Comparison of boulder displacement between experiment and *DualSPHysics* simulation.
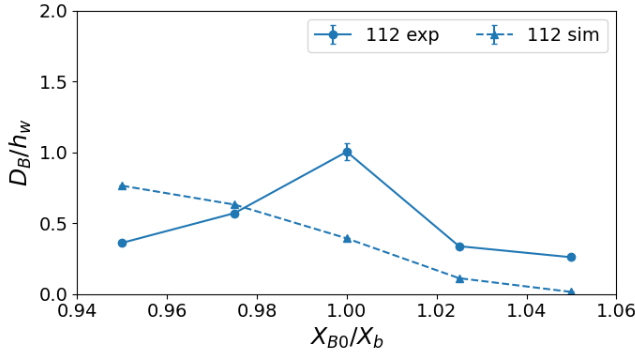

Fig. 6. Boulder 112: Comparison of boulder displacement between experiment and *DualSPHysics* simulation.

such scales are often prohibitively expensive or impractical. This section outlines the numerical setup for simulations scaled up by a factor of $S = 20$ compared to the experiments described in Section 2, and discusses the expected phenomenological differences and research objectives for these large-scale assessments.

A. Rationale and Objectives for Large-Scale Simulations

The primary motivation for extending the simulations to a larger scale is to:

1. Assess the scalability of the transport mechanisms and displacement magnitudes observed in the small-scale experiments.

2. Investigate hydrodynamic phenomena and boulder responses in a regime where inertial forces are more dominant and certain scale effects (e.g., relative influence of viscosity, surface tension if any) are diminished, aligning more closely with prototype conditions.

3. Further evaluate the robustness and performance of the DualSPHysics framework for simulating extensive coastal processes, providing insights for its application in hazard assessment for real coastal topographies and wave conditions.

4. Explore whether the conclusions drawn from small-scale studies regarding the influence of boulder geometry and initial position remain consistent at larger scales.

B. Large-Scale Numerical Experiment Setup

To achieve a 20-fold increase in physical dimensions, the parameters from the small-scale setup (Section 2) are scaled as follows:

Flume Geometry and Wave Conditions:

- **Overall Dimensions:** The numerical flume length is increased to 60 m, with a height scaled proportionally to accommodate the larger wave and water depth. The width is maintained sufficiently large or scaled to ensure predominantly two-dimensional flow characteristics in the direction of wave propagation, similar to the small-scale setup's narrow flume assumption.

- **Water Depth (h_w'):** The still water depth is increased to $h_w' = 20 \times 0.05\,\text{m} = 1.0\,\text{m}$.

- **Slope:** The $1:10$ slope is maintained. The horizontal bed section extends for $20 \times 1.65\,\text{m} = 33\,\text{m}$, and the slope's horizontal projection becomes $20 \times 1.32\,\text{m} = 26.4\,\text{m}$.

- **Solitary Wave:**
  - The wave amplitude is scaled to $a' = 20 \times 0.025\,\text{m} = 0.5\,\text{m}$. This maintains the relative wave amplitude $a'/h_w' = 0.5/1.0 = 0.5$, ensuring Froude number similarity for the incident wave conditions if wave celerity scales with $\sqrt{gh_w'}$.
  - Wave generation will continue to use the piston-type wavemaker governed by Boussinesq theory, with parameters adjusted for the new water depth and wave height.

Boulder Characteristics:

- **Dimensions:** The four boulder geometries (B111, B112, B121, B211) are geometrically scaled by $S = 20$. For example, the scaled B111 boulder (denoted B111_L) will have dimensions $L = 0.2\,\text{m}$, $W = 0.2\,\text{m}$, $H = 0.2\,\text{m}$. The scaled dimensions for all boulders are:

  - **B111_L**: $L = 0.2\,\text{m}$, $W = 0.2\,\text{m}$, $H = 0.2\,\text{m}$
  - **B112_L**: $L = 0.2\,\text{m}$, $W = 0.2\,\text{m}$, $H = 0.4\,\text{m}$
  - **B121_L**: $L = 0.2\,\text{m}$, $W = 0.4\,\text{m}$, $H = 0.2\,\text{m}$
  - **B211_L**: $L = 0.4\,\text{m}$, $W = 0.2\,\text{m}$, $H = 0.2\,\text{m}$

- **Density:** The boulder density remains $\rho_b = 2015\,\text{kg/m}^3$, representing concrete boulders at a larger scale.

- **Initial Positions:** Boulders will be placed at five initial locations, -2m, -1m, 0m, 1m, and 2m respectively, relative to the incipient wave breaking point (X_b'), maintaining the same X_{B0}/X_b' ratios as in the small-scale study ($1.0, \approx 1.025, \approx 1.05, \approx 0.975, \approx 0.95$). The actual breaking point X_b' is expected to be further offshore due to the increased water depth and wave height.

SPH Simulation Parameters:

- **Inter-Particle Spacing (d_p'):** To manage computational cost while maintaining a consistent level of detail relative to the key features, the inter-particle spacing will be scaled by $S = 20$. Given the small-scale $d_p = 0.00125\,\text{m}$ (which yielded $H/d_p = 20$ for the 0.025m wave amplitude), the large-scale $d_p' = 20 \times 0.00125\,\text{m} = 0.025\,\text{m}$. This ensures

that the number of particles resolving the wave height ($a'/d_p' = 0.5/0.025 = 20$) and the characteristic height of the boulders (e.g., $H_{\text{B111\_L}}/d_p' = 0.2/0.025 = 8$) remains the same as in the validated small-scale simulations. This scaling strategy implies that the total number of particles in the simulation domain will be approximately similar to the small-scale setup, making these large-scale simulations computationally feasible.

- **Smoothing Length (h'):** Scaled proportionally to d_p'.

- **Viscosity and Density Diffusion:** The artificial viscosity coefficient $\alpha = 0.025$ and the density diffusion parameters (full Fourtakas model, coefficient 0.1) will be initially retained, consistent with recommendations for large-scale coastal modeling [21] and the findings from the small-scale simulations. Sensitivity to these parameters at the larger scale may be a subject for future investigation.

- **Time Stepping and Simulation Duration:** The CFL condition and other numerical settings (e.g., Wendland kernel, mDBC) will be applied as in the small-scale study. The total simulation time will be adjusted to capture the full extent of boulder transport, considering that wave celerity scales approximately with $\sqrt{S}$ and characteristic transport times may also scale.

A total of 20 distinct simulation cases will be conducted for the large-scale scenario, mirroring the combinations of four boulder types and five initial positions.

Table 1. Comparison of primary parameters between the small-scale (validated) and large-scale numerical experiments.

Parameter	Small-Scale	Large-Scale (20x)	Unit
Flume Length	3	60	m
Water Depth (h_w)	0.05	1.0	m
Wave Amplitude (a)	0.025	0.5	m
a/h_w	0.5	0.5	-
Boulder B111 H	0.01	0.2	m
Boulder Density (ρ_b)	2015	2015	kg/m^3
Particle Spacing (d_p)	0.00125	0.025	m
a/d_p	20	20	-
H_{B111}/d_p	8	8	-

C. Simulation Execution and Boulder Displacement Analysis Focus for Large-Scale Scenarios

The 20 large-scale simulations were executed following the setup detailed in Section B. The primary analysis focuses on comparing the final displacement of each boulder against the scaled results from the small-scale experiments to quantitatively assess the impact of scale on transport dynamics. The results and analysis for each of the four boulder geometries are presented below.

For the cubic **B111_L boulder**, the displacement in the large-scale simulations shows a trend that is qualitatively similar to the small-scale results, as seen in Figure 7. However, the large-scale model predicts a slightly lower final displacement. This is likely due to the increased energy dissipation that occurs as

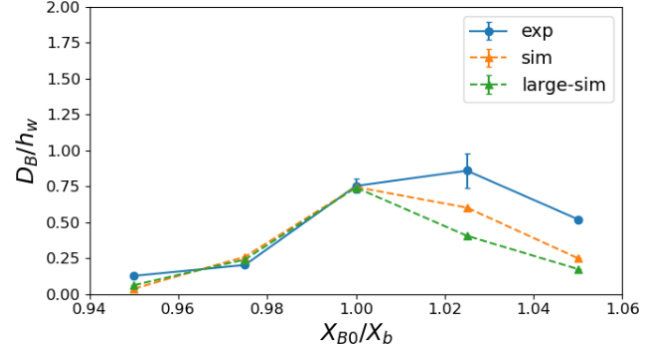the larger wave propagates over the proportionally longer beach slope before impacting the boulder.

Fig. 7. Comparison of boulder displacement for the B111 boulder between small-scale and large-scale simulations.

The **B211_L boulder**, which is elongated in the direction of flow, also behaves consistently with its small-scale counterpart (Figure 8). The phenomenon of the wave's breaking point shifting further offshore due to the boulder's geometry is replicated in the large-scale simulation, confirming that this specific fluid-structure interaction scales up effectively.
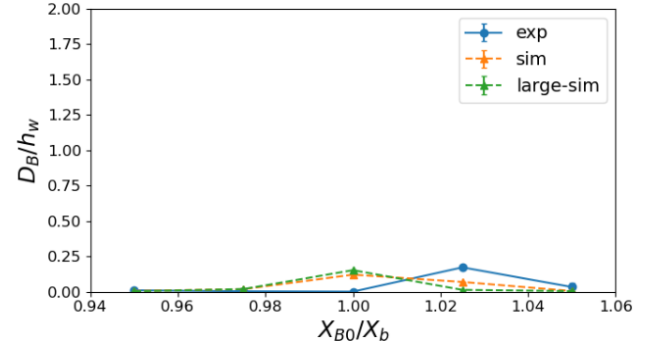

Fig. 8. Comparison of boulder displacement for the B211 boulder between small-scale and large-scale simulations, showing consistent breaking point shift.

The analysis for the wide **B121_L boulder**, shown in Figure 9, reveals a behavior that aligns well with the small-scale simulations, especially for placements before the wave breaking point. For initial positions at and beyond the breaking point ($X_{B0}/X_b' \geq 1.0$), the increased wave travel distance over the slope in the large-scale model leads to greater energy dissipation, resulting in a more pronounced reduction in transport compared to the scaled predictions.

Most significantly, the tall **B112_L boulder** demonstrates a critical difference between the simulation scales (Figure 10). While the small-scale numerical results for this shape diverged from physical expectations, the large-scale simulation correctly predicts the displacement trend. This outcome suggests that the large-scale model more accurately captures the dominant physical forces, overcoming potential scale effects related to viscosity or turbulence modeling that may have distorted the small-scale numerical results for this slender geometry.

The findings from these large-scale simulations will be crucial for understanding the limitations of direct extrapolation from small-scale experiments and for enhancing the predictive capabilities of SPH models for real-world coastal hazard assessments.
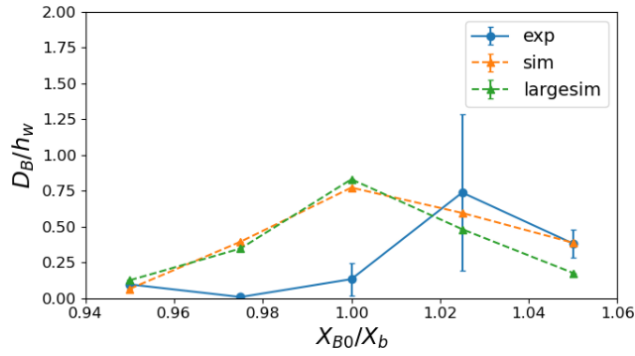
Fig. 9. Comparison of boulder displacement for the B121 boulder between small-scale and large-scale simulations.
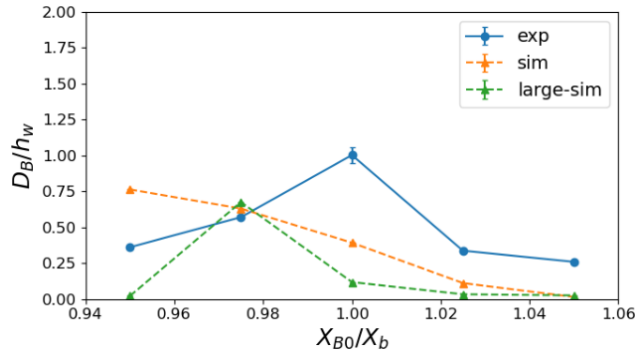

Fig. 10. Comparison of boulder displacement for the B112 boulder, highlighting the improved accuracy of the large-scale simulation.

6. DISCUSSION

As observed, the numerical resolution has a notable impact on the intersection between the water surface and the sloping bed, which in turn may influence the precise location of wave breaking. In the large-scale simulations, the resolution relative to the primary features (e.g., particles per wave height) was kept consistent with the small-scale study. While computationally pragmatic, this scaling of the inter-particle spacing (d_p) means that certain small-scale physical effects may have been automatically smoothed out or ignored due to the insufficient resolution at that scale, rather than as a consequence of natural physical scaling phenomena where inertial forces dominate over viscous ones. It raises the question of whether improved model-experiment agreement in some large-scale cases is due to the model correctly capturing prototype physics or from the numerical filtering of complex small-scale behaviors that the model struggled to resolve. Therefore, further investigation is required to determine how the resolution at the fluid-boundary intersection consistently alters wave breaking and hydrodynamics. A systematic sensitivity analysis, utilizing highly refined meshes for both small- and large-scale scenarios, is recommended for future work. Such an approach would help to decouple numerical artifacts from physical scale effects and clarify the influence of the smoothing length and particle spacing on the accuracy of wave propagation and boulder transport predictions.

Regarding the overturning behavior of boulders, the current single-phase SPH approach may not adequately capture the complex fluid–solid interaction involved. Introducing a two-phase SPH solver [20], where air and water phases are treated sepa-

rately, could offer a more realistic representation of wave breaking dynamics and boulder-fluid coupling. Such an approach could be particularly beneficial in resolving air entrainment effects, impact pressure distribution, and rotational motion during overturning events.

7. CONCLUSION

In this study, we validated the *DualSPHysics* solver. For this, we conducted a comparative analysis of boulder transport behavior for four different boulder configurations (111, 112, 121, and 211). The results show that, in most cases, the numerical model successfully reproduced the displacement trends observed in the experiments. Although discrepancies were observed—particularly for boulders 121 and 112 near the wave breaking region—these differences are likely due to the sensitivity of SPH simulations to particle resolution, initial positioning, and local hydrodynamic complexity.

The extension of this study to large-scale scenarios further reinforced these findings, revealing that the fundamental transport mechanisms scale in a consistent manner. A pivotal outcome of the large-scale assessment was the simulation of the B112 boulder. While the small-scale simulation for this geometry showed significant deviation from experimental trends, the large-scale model successfully predicted the transport behavior, aligning closely with the physical dynamics expected at that scale. This result is particularly encouraging, as it suggests that at prototype scales where certain scale effects are less pronounced, the SPH model can overcome limitations observed in laboratory-scale simulations.

Overall, this work demonstrates the capability of Smoothed Particle Hydrodynamics (SPH) to replicate experimental hydrodynamics and sediment transport in a fully Lagrangian framework. By validating SPH models at a small scale and confirming their applicability at a larger scale, we establish a solid foundation for their use in complex coastal scenarios. This approach enables systematic parametric studies and predictive modeling under controlled digital environments.

Looking forward, this study highlights the potential of SPH as a practical and cost-effective tool for simulating wave–structure interactions and assessing coastal hazards. It indicates a strong potential for *DualSPHysics* to accurately predict boulder transport in natural, large-scale coastal environments. Future work should focus on employing increasingly refined resolutions, incorporating two-phase solvers to better capture wave breaking, and introducing SPH models that account for surface tension[35] to more accurately describe small-scale physical effects. These advancements will further enhance the accuracy of boulder transport predictions, especially in the highly dynamic regions near wave breaking and in the context of laboratory-scale validation.

FULL REFERENCES

1. S. Iwai, K. Goto, and T. Ishizawa, "A gigantic boulder transported by the 2011 tohoku-oki tsunami," Island Arc **28**, e12321 (2019).

2. R. Cox, F. Ardhuin, F. Dias, *et al.*, "Systematic review shows that work done by storm waves can be misinterpreted as tsunami-related because commonly used hydrodynamic equations are flawed," Front. Mar. Sci. **7** (2020).

3. F. Imamura, K. Goto, and S. Ohkubo, "A numerical model for the transport of a boulder by tsunami," J. Geophys. Res. Ocean. **113** (2008). Cited by: 214; All Open Access, Bronze Open Access.

4. J. Oetjen, M. Engel, and H. Schüttrumpf, "Experiments on tsunami induced boulder transport – a review," Earth-Science Rev. **220**, 103714 (2021).

5. H. A. Lodhi, H. Hasan, and N. Nandasena, "The role of hydrodynamic impact force in subaerial boulder transport by tsunami—experimental evidence and revision of boulder transport equation," Sediment. Geol. **408**, 105745 (2020).

6. J. N. Steer, O. Kimmoun, and F. Dias, "Breaking-wave induced pressure and acceleration on a clifftop boulder," J. Fluid Mech. **929**, R1 (2021).

7. A. Zainali and R. Weiss, "Boulder dislodgement and transport by solitary waves: Insights from three-dimensional numerical simulations," Geophys. Res. Lett. **42**, 4490 – 4497 (2015). Cited by: 23.

8. J. Stolle, I. Nistor, N. Goseberg, *et al.*, "Entrainment and transport dynamics of shipping containers in extreme hydrodynamic conditions," Coast. Eng. J. **59**, 1750011 (2017).

9. N. Nandasena and N. Tanaka, "Boulder transport by high energy: Numerical model-fitting experimental observations," Ocean. Eng. **57**, 163–179 (2013).

10. J. Stolle, T. Takabatake, G. Hamano, *et al.*, "Debris transport over a sloped surface in tsunami-like flow conditions," Coast. Eng. J. **61**, 241–255 (2019).

11. K. D. Goral, H. G. Guler, C. Baykal, and A. C. Yalciner, "An experimental study on the motion of solid spheres under solitary wave attack," Ocean. Eng. **240**, 109946 (2021).

12. J. Oetjen, M. Engel, S. P. Pudasaini, and H. Schuettrumpf, "Significance of boulder shape, shoreline configuration and pre-transport setting for the transport of boulders by tsunamis," Earth Surf. Process. Landforms **45**, 2118–2133 (2020).

13. P.-T. Su, I. Didenkulova, and A. Jensen, "Solitary wave-induced boulder transport on a beach," Ocean. Eng. **313**, 119318 (2024).

14. L. B. Lucy, "A numerical approach to the testing of the fission hypothesis." Astron. J. **82**, 1013–1024 (1977).

15. R. Dalrymple and B. Rogers, "Numerical modeling of water waves with the sph method," Coast. Eng. **53**, 141–147 (2006). Coastal Hydrodynamics and Morphodynamics.

16. A. Crespo, C. Altomare, J. Domínguez, *et al.*, "Towards simulating floating offshore oscillating water column converters with smoothed particle hydrodynamics," Coast. Eng. **126**, 11–26 (2017).

17. A. Crespo, J. Domínguez, B. Rogers, *et al.*, "Dualsphysics: Opensource parallel cfd solver based on smoothed particle hydrodynamics (sph)," Comput. Phys. Commun. **187**, 204–216 (2015).

18. J. M. Domínguez, G. Fourtakas, C. Altomare, *et al.*, "DualSPHysics: from fluid dynamics to multiphysics problems," Comput. Part. Mech. **9**, 867–895 (2022).

19. V. Zago, L. Schulze, G. Bilotta, *et al.*, "Overcoming excessive numerical dissipation in sph modeling of water waves," Coast. Eng. **170**, 104018 (2021).

20. Y. Zhan, M. Luo, and A. Khayyer, "Dualsphysics+: An enhanced dualsphysics with improvements in accuracy, energy conservation and resolution of the continuity equation," Comput. Phys. Commun. **306**, 109389 (2025).

21. C. Altomare, P. Scandura, I. Cáceres, *et al.*, "Large-scale wave breaking over a barred beach: Sph numerical simulation and comparison with experiments," Coast. Eng. **185**, 104362 (2023).

22. D. G. Goring, "Tsunamis – the propagation of long waves onto a shelf," Ph.D. dissertation, California Institute of Technology (1979).

23. J. M. Domínguez, C. Altomare, J. Gonzalez-Cao, and P. L. and, "Towards a more complete tool for coastal engineering: solitary wave generation, propagation and breaking in an sph-based model," Coast. Eng. J. **61**, 15–40 (2019).

24. Altomare, Corrado and González-Cao, J. and Domínguez, J.M. and Crespo, A.J.C and Gómez-Gesteira, M. and Lomonaco, Pedro, "Generation of trains of tsunami-like solitary waves in DualSPHysics model," (2017), pp. 83–90.

25. J. M. Domínguez, A. J. Crespo, M. Hall, *et al.*, "Sph simulation of floating structures with moorings," Coast. Eng. **153**, 103560 (2019).

26. H. Wendland, "Piecewise polynomial, positive definite and compactly supported radial functions of minimal degree," **4**, 389–396.

27. B. Leimkuhler and C. Matthews, "Molecular dynamics: With deterministic and stochastic numerical methods." Interdiscip. applied mathematics **39** (2015).

28. C. Altomare, A. J. Crespo, J. M. Domínguez, *et al.*, "Applicability of smoothed particle hydrodynamics for estimation of sea wave impact on coastal structures," Coast. Eng. **96**, 1–12 (2015).

29. G. Fourtakas, R. Vacondio, J. Dominguez Alonso, and B. Rogers, "Improved density diffusion term for long duration wave propagation," (2020), pp. 351–357. 2020 SPHERIC Harbin International Workshop ; Conference date: 13-01-2020 Through 16-09-2020.

30. P. Sun, A. Colagrossi, S. Marrone, *et al.*, "A consistent approach to particle shifting in the -plus-sph model," Comput. Methods Appl. Mech. Eng. **348**, 912–934 (2019).

31. A. English, J. M. Domínguez, R. Vacondio, *et al.*, "Modified dynamic boundary conditions (mDBC) for general-purpose smoothed particle hydrodynamics (SPH): application to tank sloshing, dam break and fish pass problems," **9**, 1–15.

32. I. Martínez-Estévez, J. Domínguez, B. Tagliafierro, *et al.*, "Coupling of an sph-based solver with a multiphysics library," Comput. Phys. Commun. **283**, 108581 (2023).

33. Engineers Edge, "Coefficients of friction chart table for dry concrete," https://www.engineersedge.com/physics/physics-master/notes/force/friction/index.html (2025). Accessed: June 6, 2025.

34. N. Khun, P. Loong, E. Liu, and L. Li, "Enhancing electrical and tribological properties of poly(methyl methacrylate) matrix nanocomposite films by co-incorporation of multiwalled carbon nanotubes and silicon dioxide microparticles," J. Polym. Eng. **36**, 23–30 (2016).

35. C. Cen, G. Fourtakas, S. Lind, and B. D. Rogers, "A single-phase gpu-accelerated surface tension model using sph," Comput. Phys. Commun. **295**, 109012 (2024).